GI2T/REGAIN spectro-interferometry with a new infrared beam combiner

G. Weigelt[a], D. Mourard[b], L. Abe[b], U. Beckmann[a],
O. Chesneau[a], C. Hillemanns[a], K.-H. Hofmann[a], S. Ragland[b],
D. Schertl[a], M. Scholz [c], P. Stee[b], N. Thureau[b], F. Vakili[b]

[a]MPI für Radioastronomie, Auf dem Huegel 69, 53121 Bonn, Germany
[b]Departement Fresnel, CNRS/UMR 6528, Observatoire de la Cote d'Azur,
2130, route de l'Observatoire, Caussols, 06460 St Vallier de Thiey, France
[c]Institut für Theoretische Astrophysik der Universitaet Heidelberg,Tiergartenstrasse 15,
69121 Heidelberg, Germany

ABSTRACT

We have built an infrared beam combiner for the GI2T/REGAIN interferometer of the Observatoire de la Cote d'Azur. The beam combiner allows us to record spectrally dispersed Michelson interference fringes in the near-infrared J-, H- or K-bands. The beam combiner has the advantage that Michelson interferograms can simultaneously be recorded in about 128 different spectral channels. The tilt of the spectrally dispersed fringes is a measure of the instantaneous optical path difference. We present the optical design of the beam combiner and GI2T/REGAIN observations of the Mira star R Cas with this beam combiner in the spectral range of 2.00 μm – 2.18 μm (observations on 22 and 25 August 1999; variability phase 0.08; V-magnitude approximately 6; seven baselines between 12 m and 24 m; reference stars Vega and β Peg). The spectrograph of the beam combiner consists of an anamorphotic cylindrical lens system, an image plane slit, and a grism. The detector is a 256x256 pixel Rockwell PICNIC array camera. The shortest possible exposure time is 10 ms. A system of digital signal processors calculates the ensemble average power spectrum of the spectrally dispersed Michelson interferograms, the instantaneous optical path difference error, and several other useful parameters in real time. From the observed R Cas visibilities at baselines 12.0 m, 13.8 m and 13.9 m, a 2.1 μm uniform-disk diameter of 25.3 mas $\pm$ 3.3 mas was derived. The unusually high visibility values at baselines $\geq$ 16 m show that the stellar surface of R Cas is more complex than previously assumed. The visibility values at baselines $\geq$ 16 m can be explained by high-contrast surface structure on the stellar surface of R Cas or other types of unexpected center-to-limb variations. The R Cas observations were compared with theoretical Mira star models[1,2]. We obtained the following results for R Cas at variablity phase 0.08:
Angular Rosseland radius R^a: 12.1 mas $\pm$ 1.7 mas
Linear Rosseland radius R: 276 $R_\odot$ $\pm$66 $R_\odot$ (using the HIPPARCOS parallax of 9.36 mas $\pm$1.10 mas)
Effective temperature: 2685 K $\pm$ 238 K (derived from the angular Rosseland radius and the JHKLM-photometry).

Keywords: interferometry - infrared - spectroscopy - evolved stars - Mira stars

1. INTRODUCTION

The GI2T/REGAIN interferometer[3,4] is an optical interferometer of two 1.5 m telescopes. For this interferometer we have built an infrared beam combiner and used it to record spectrally dispersed infrared Michelson interferograms of the Mira star R Cas. In this paper we present the design of our new infrared beam combiner and R Cas observations obtained in August 1999. This beam combiner allows us to simultaneously record Michelson fringes in about 128 different spectral channels from 2.00 to 2.18 μm. The tilt of the spectrally dispersed fringes is a measure of the instantaneous optical path difference. The R Cas observations reported in this paper are the first NIR interferometry observations with large 1.5 m telescopes. The aim of our Mira star project is to resolve the stellar disk of Mira stars, to reveal photospheric asymmetries and surface structures, and to study the wavelength and phase dependence of the diameter. Previous speckle or long-baseline interferometry observations of Mira stars were, for example, reported in Refs. 5-16. Theoretical studies[1,2,17–19] show that interferometric diameter measurements can considerably improve our understanding of cool stellar atmospheres.

2. INSTRUMENT

Figure 1 shows the optical layout of our new NIR beam combiner built at the MPI for Radioastronomy. It consists of an anamorphotic lens system, an image plane slit, a grism, a shutter, a PICNIC detector, a data storage computer, and an array of digital signal processors for data processing. The DSPs can calculate the power spectrum and the instantaneous optical path difference in real-time. The typical frame rate is 3 frames per second (256×256 pixels per frame).

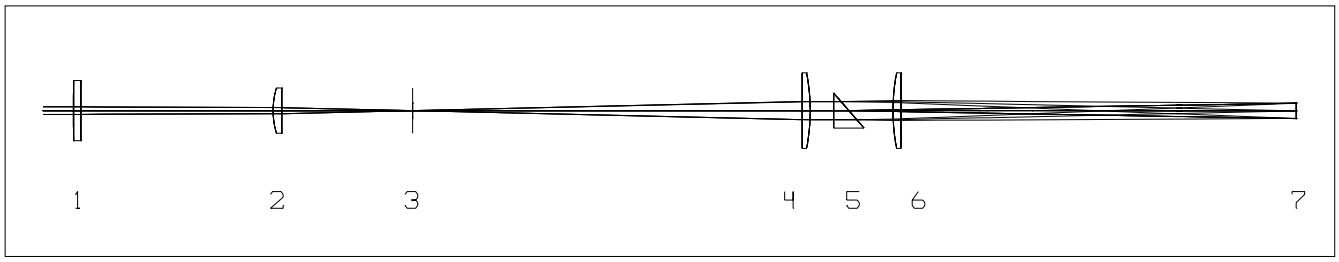

Figure 1. Optical layout of the new NIR beam combiner (1 beam combiner lens with 750 mm focal length; 2, 4 and 6 cylindrical lenses; 3 image plane slit and slit viewer camera; 5 grism; 7 PICNIC detector; anamorphotic compression factor 9).

3. R CAS OBSERVATIONS AND DATA PROCESSING

The first infrared observations with our new beam combiner mounted to the GI2T/REGAIN interferometer were carried out on August 22 and 25, 1999. The observational parameters of the R Cas and reference star observations are as follows:

Projected R Cas baselines:	12.01 m, 13.80 m, 13.88 m, 18.14 m, 19.79 m, 21.99 m, 23.79 m
Date of R Cas observations:	22 Aug. 1999 (baselines 12.01 m, 13.80 m),
	25 Aug. 1999 (baselines 13.88 m, 18.14 m, 19.79 m, 21.99 m, 23.79 m)
Reference stars:	Vega, β Peg
Number of frames per baseline:	500
Frame rate:	3 frames/s
Filter:	center wavelength 2.1 μm, FWHM bandwidth 0.3 μm
Recorded wavelength band:	2.00 μm – 2.18 μm
Number of spectroscopic channels:	128
Anamorphotic projection factor:	9
Exposure time per frame:	100 ms
K-band seeing:	2 arcsec

Figure 2 shows two of several thousand recorded interferograms of R Cas. The interferograms of R Cas and the reference stars were flatfielded and sky-subtracted, and the visibilities of each spectral channel and baseline were derived by calculating the ensemble average power spectra. The method described by Mourard et al.[20] was applied to derive visibility ratios of the object and reference star observations and to obtain calibrated R Cas visibilities. Figure 3 shows the derived R Cas visibilities. The solid line is the visibility function of a uniform-disk of a star with 25.3 mas diameter. The dashed curve is the uniform-disk visibility fit curve which is required for our observations with large 1.5 m telescopes. This dashed visibility fit function has no zeros since an average of many baselines is measured rather than only one single baseline if the telescope pupils are large. If the projected baseline from mirror center to mirror center is for example 10 m, all baselines between 8.5 m and 11.5 m are simultaneously measured. The

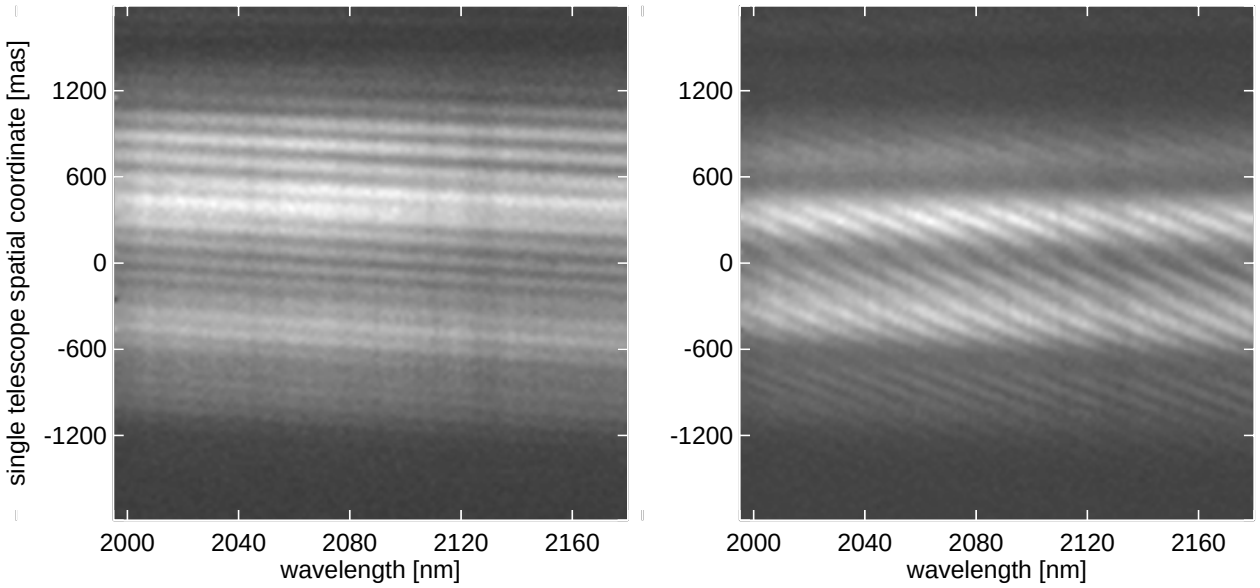

Figure 2. Two of several thousand recorded interferograms of the Mira star R Cas (spectral range 2.00 to 2.18 μm; baseline 13.80 m). In the left interferogram the fringes are nearly parallel to the dispersion direction since the optical path difference error is almost zero. In the right interferogram the fringes are tilted due to a small optical path difference error.

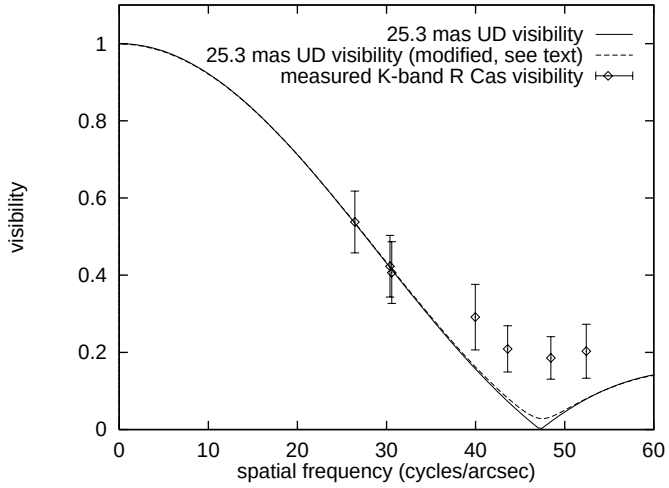

Figure 3. GI2T/REGAIN visibility measurements of R Cas with our new NIR beam combiner (baselines 12.01 m, 13.80 m, 13.88 m, 18.14 m, 19.79 m, 21.99 m, 23.79 m).

R Cas visibilities in Fig. 3 show that the center-to-limb variation of R Cas is not a uniform-disk function. The large visibility values at spatial frequencies larger than ~ 40 cycles per arcsec can be explained by high-contrast surface structure on the stellar surface of R Cas or by other types of unexpected center-to-limb variations. A uniform-disk fit diameter of 25.3 mas $\pm$ 3.3 mas is obtained if only the first three low-frequency visibility points (projected baselines 12.01 m, 13.80 m, and 13.88 m) are used for the uniform-disk fit. The error bars of our first IR observations

are relatively large because the weather situation was not favorable and the control system (Mourard et al., this proceedings[21]) of the GI2T/REGAIN (Mourard et al., this proceedings[22]) was not fully operational. Under normal observing conditions the error bars will be much smaller.

4. COMPARISON OF THE OBSERVATIONS WITH MIRA STAR MODELS

4.1. The stellar filter radius and Rosseland radius of R Cas

In this section we derive various types of angular diameters from the measured visibilities of R Cas by applying the different theoretical center-to-limb intensity variations (hereafter CLV) of different Mira star models (Bessel, Scholz, and Wood 1996 = BSW96[1], Hofmann, Scholz and Wood 1998 = HSW98[2]). From these angular diameters (Fig. 4) and the bolometric flux, we derive effective temperatures (Fig. 6). All Mira star models used in this paper are from BSW96 (D and E series) and from HSW98 (P, M and O series). They were developed as possible representations of the prototype Mira variable o Ceti, and hence have periods P very close to the 332 day period of this star. They differ in pulsation mode, assumed mass M and assumed luminosity L. The BSW96 models differ from the more advanced HSW98 models with respect to the pulsation modelling technique. The five models represent stars pulsating in the fundamental mode (f; D, P and M models) or in the first-overtone mode (o; E and O models). Table 1 lists the properties of these Mira model series. Table 2 provides the link between the 22 abscissa values (model-phase combinations m) in Figs. 4 - 6, and the models. $R_{\rm p}$ denotes the Rosseland radius (below) of the non-pulsating parent star of the Mira variable (BSW96, HSW98). Table 2 additionally lists the variability phase, the relative Rosseland and stellar K-band radius, and the effective temperature. We compare predictions of these models for different phases and cycles with our observations.

Monochromatic radius R_λ and Rosseland radius R. We use the conventional stellar radius definition where the monochromatic radius R_λ of a star at wavelength λ is given by the distance from the star's center at which the optical depth equals unity ($\tau_\lambda = 1$). In analogy, the photospheric stellar radius R (Rosseland radius) is given by the distance from the star's center at which the Rosseland optical depth equals unity ($\tau_{\rm Ross} = 1$). This radius has the advantage of agreeing well (see Table 6 in HSW98 for deviations sometimes occurring in very cool stars) with measurable near-infrared continuum radii and with the standard boundary radius of pulsation models with $T_{\rm eff} \propto (L/R^2)^{1/4}$.

Stellar filter radius $R_{\rm f}$. For the K-band filter used for the observations, we have calculated the theoretical CLVs of the above mentioned five Mira star models at different phases and cycles. The stellar radius for filter transmission f_λ is the intensity- and filter-weighted radius $R_{\rm f} = \int R_\lambda\, I_\lambda\, f_\lambda\, d\lambda / \int I_\lambda\, f_\lambda\, d\lambda$, which we call *stellar filter radius* $R_{\rm f}$ after Scholz & Takeda's definition[23]. In this equation R_λ denotes the above monochromatic $\tau_\lambda = 1$ radius, I_λ the central intensity spectrum and f_λ the transmission of the filter.

4.2. Angular R Cas radii

The observed angular stellar K-band radii $R^a_{\rm K,m}$ of R Cas corresponding to the various model-phase combinations m, were derived by least-squares fits between the first three visibility values (baselines 12.01 m, 13.80 m and 13.88 m) shown in Fig. 3 and the visibilities of the different theoretical K-band CLVs of different model-phase combinations m. Additionally, the observed angular Rosseland radii $R^a_{\rm m}$ of R Cas corresponding to the model-phase combination m were derived from the observed angular stellar K-band radii $R^a_{\rm K,m}$ and the theoretical radius ratios $R_{\rm m}/R_{\rm K,m}$ from Table 2 (Table 2 provides theoretical R and $R_{\rm K}$ values for each model-phase combination m). The derived angular stellar filter radii $R_{\rm K,m}$ and angular Rosseland radii $R_{\rm m}$ are shown in Fig. 4.

Table 1. Properties of Mira model series[1,2] (see text)

Series	Mode	P(days)	$M/M_\odot$	$L/L_\odot$	$R_{\rm p}/R_\odot$	$T_{\rm eff}$/K
D	f	330	1.0	3470	236	2900
E	o	328	1.0	6310	366	2700
P	f	332	1.0	3470	241	2860
M	f	332	1.2	3470	260	2750
O	o	320	2.0	5830	503	2250

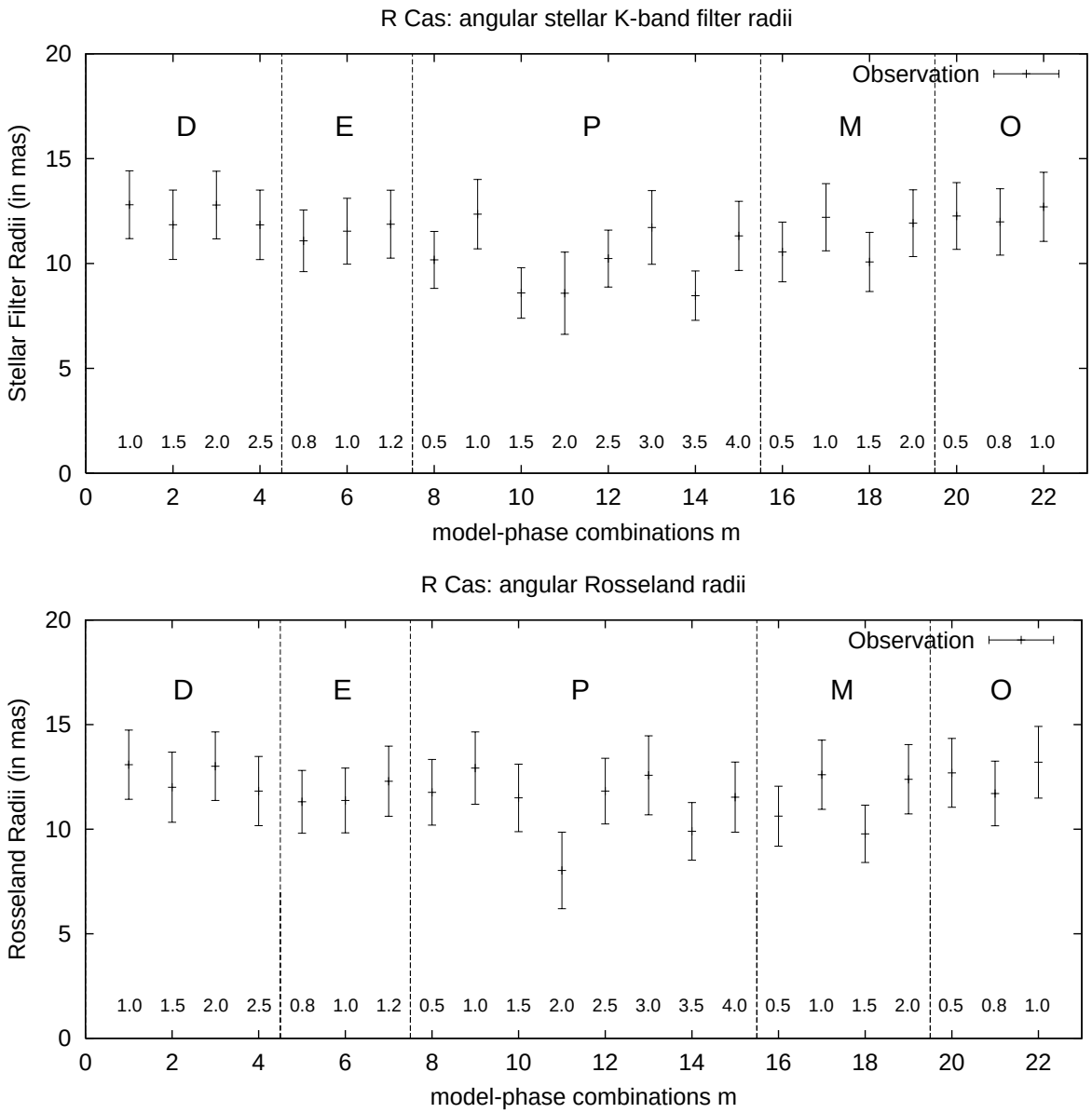

Figure 4. Observed angular stellar K-band radii $R^a_{\mathrm{K,m}}$ (top) and Rosseland radii R^a_{m} (bottom) of R Cas derived from the measured R Cas visibilities by fitting the theoretical CLVs of the 22 model-phase combinations m. Table 2 shows the link between the abscissa values and the models and the variability phases.

Table 2. Link between the 22 model-phase combinations m in Figs. 4 - 6, and the models. The variability phase $\Phi_{\rm vis}$, the Rosseland radius R and the K-band radius $R_{\rm K}$ in units of the non-pulsating parent star radius R_p (see BSW96), and the effective temperature $T_{\rm eff}(R)$ associated to the Rosseland radius are additionally given.

Model	$\Phi_{\rm vis}$	$R/R_{\rm p}$	$R_{\rm K}/R_{\rm p}$	$T_{\rm eff}(R)$	m
D27520	1+0.0	1.04	1.02	3020	1
D27760	1+0.5	0.91	0.90	2710	2
D28760	2+0.0	1.04	1.02	3030	3
D28960	2+0.5	0.91	0.91	2690	4
E8300	0+0.83	1.16	1.14	2330	5
E8380	1+0.0	1.09	1.10	2620	6
E8560	1+0.21	1.17	1.14	2610	7
P71800	0+0.5	1.20	1.04	2160	8
P73200	1+0.0	1.03	0.99	3130	9
P73600	1+0.5	1.49	1.12	1930	10
P74200	2+0.0	1.04	1.11	3060	11
P74600	2+0.5	1.17	1.02	2200	12
P75800	3+0.0	1.13	1.06	3060	13
P76200	3+0.5	1.13	0.96	2270	14
P77000	4+0.0	1.17	1.14	2870	15
M96400	0+0.5	0.93	0.92	2310	16
M97600	1+0.0	1.19	1.15	2750	17
M97800	1+0.5	0.88	0.90	2460	18
M98800	2+0.0	1.23	1.19	2650	19
O64210	0+0.5	1.12	1.09	2050	20
O64530	0+0.8	0.93	0.95	2150	21
O64700	1+0.0	1.05	1.01	2310	22

4.3. Linear R Cas radii

We have derived linear stellar radii of R Cas (in units of solar radii) from the measured angular stellar K-band radii $R^a_{\rm K,m}$ and Rosseland radii $R^a_{\rm m}$ (Fig. 4) by using the R Cas HIPPARCOS parallax of $9.36\,{\rm mas} \pm 1.10\,{\rm mas}$[24]. Fig. 5 shows the obtained R Cas radii for all model-phase combinations m. The theoretical Rosseland radii of the M and of the P model series at nearly all available near-maximum phases (1.0, 3.0, 4.0) are close (within the error bars) to the measured Rosseland radii. The theoretical Rosseland radii of the first-overtone models E and O are clearly too large compared with measured Rosseland radii. The theoretical radii of the D model series are slightly too small compared with the measured Rosseland radii. The same conclusions are also valid for the linear stellar filter radii $R_{\rm K}$ (Fig. 5).

If we calculate average linear radii by averaging the radii obtained with all available *near-maximum* M models (i.e., m = 17, 19) and/or *near-maximum* P models (i.e., m = 9, 11, 13, 15) we obtain:

Average theoretical M model Rosseland radius: $315\,{\rm R}_\odot$

Average measured M model Rosseland radius: $287\,{\rm R}_\odot \pm 51\,{\rm R}_\odot$ (obtained with m = 17 and 19)

Average theoretical P model Rosseland radius: $263\,{\rm R}_\odot$

Average measured P model Rosseland radius: $264\,{\rm R}_\odot \pm 82\,{\rm R}_\odot$ (obtained with m = 9, 11, 13 and 15)

Average theoretical model Rosseland radius: $289\,{\rm R}_\odot$

Average measured model Rosseland radius: $276\,{\rm R}_\odot \pm 66\,{\rm R}_\odot$ (m = 9, 11, 13, 15, 17, 19; M and P models)

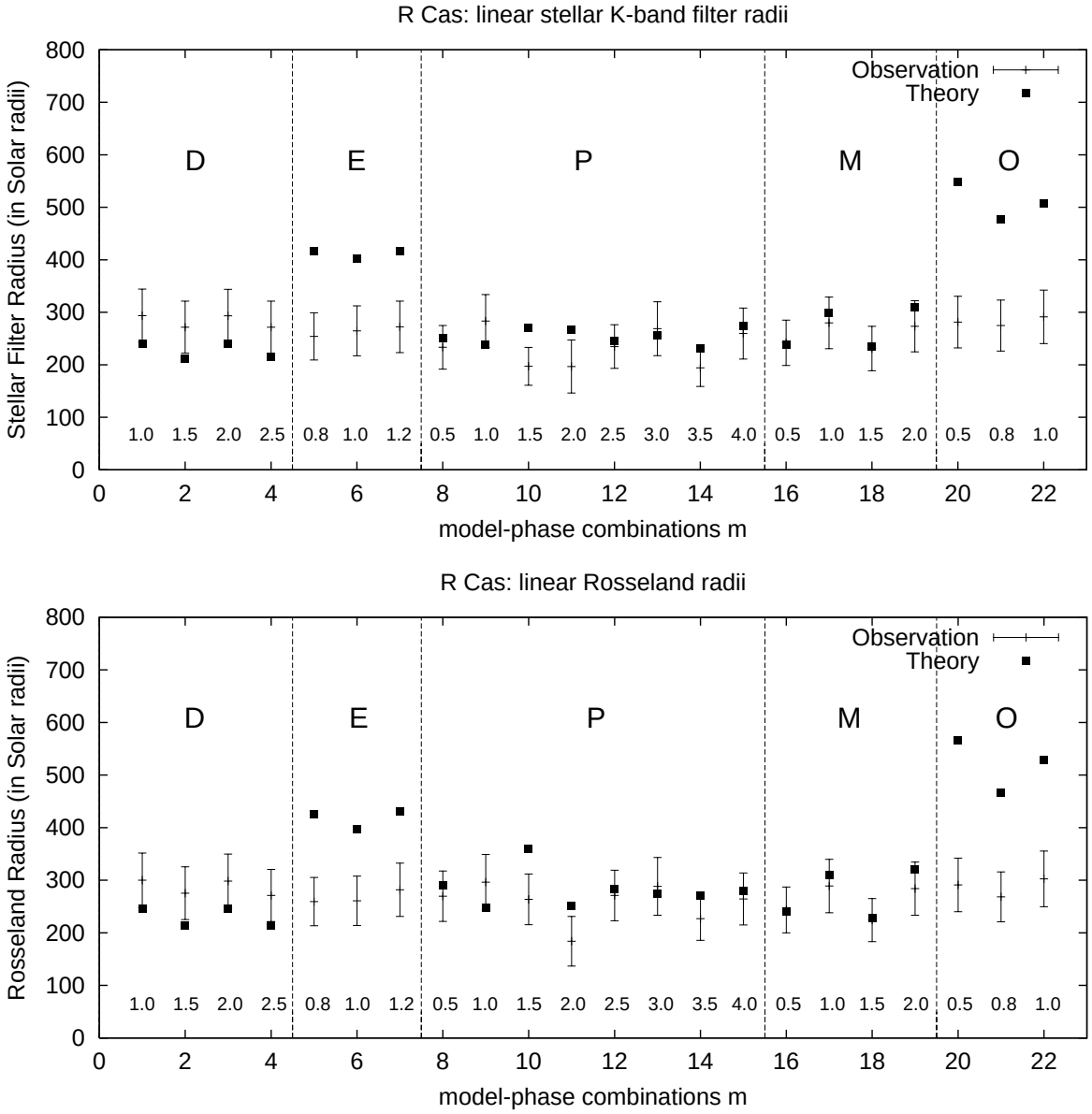

Figure 5. Comparison of observed R Cas radii (crosses; see Sect. 4.3) and theoretical model radii (filled squares; D, E, P, M and O model for different phases; see Table 2) plotted versus all 22 model-phase combinations m (top: stellar K-band radii $R_{\mathrm{K,m}}$; bottom: Rosseland radii R_{m}).

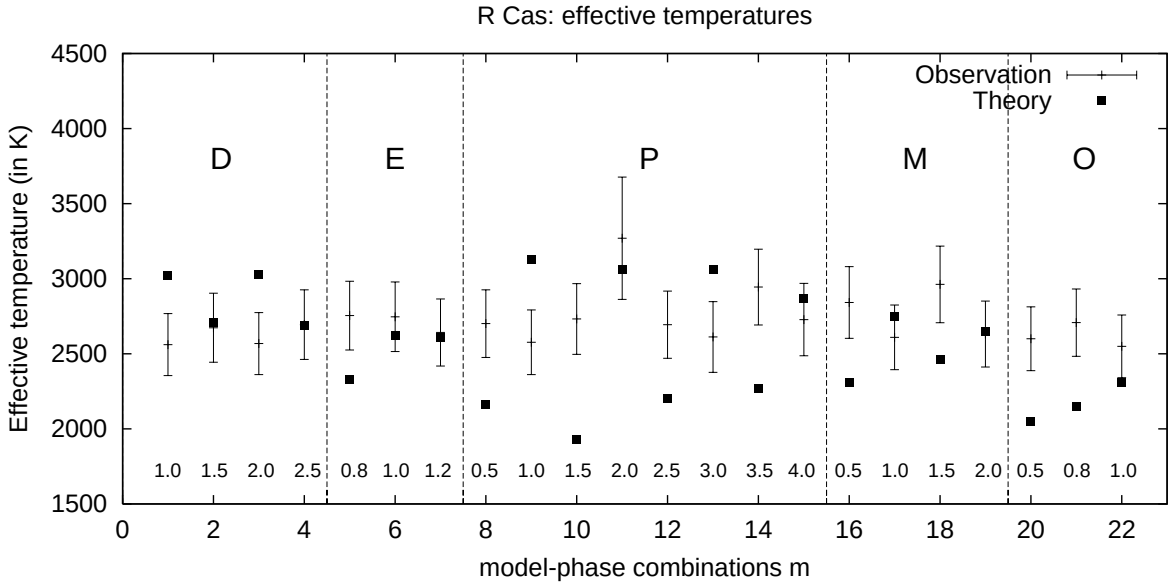

Figure 6. Comparison of model effective temperatures $T_{\rm eff,m}$ (plotted versus the 22 model-phase combinations m; see Sect. 4.1) and the measured R Cas effective temperatures derived from measured angular Rosseland radii $R^a_{\rm m}$ (see Sect. 4.2) and JHKLM-photometry. Table 2 shows the link between the abscissa values m and the models and phases.

4.4. Effective temperatures of R Cas

Effective temperatures of R Cas were derived from its angular Rosseland radii $R^a_{\rm m}$ (Sect. 4.2) and its bolometric flux using the relation

$$T_{\rm eff} = 2341 \text{ K} \times (F_{\rm bol}/\phi^2)^{1/4}, \quad (1)$$

where $F_{\rm bol}$ is the apparent bolometric flux in units of $10^{-8}\,{\rm erg\,cm^{-2}\,s^{-1}}$ and $\phi = 2\,R^a_{\rm m}$ is the angular Rosseland diameter in mas. The bolometric flux was derived from JHKLM-band observations carried out 7 days after the visibility observations. For cool stars such as LPVs, where most of the luminosity is emitted at near-infrared wavelengths, a convenient approximation for calculating bolometric magnitudes is to use a blackbody function to interpolate between photometric observations in the J, H, K, L and M bands. For estimating the bolometric flux we used the photometric JHKLM measurements of B. Yudin which were carried out with the 1.25 m telescope at the Crimean station of the Sternberg Astronomical Institute in Moscow seven days after our visibility observations. The derived bolometric flux of R Cas on 29 August 1999 was $980.6\pm180 \times 10^{-8}\,{\rm erg\,cm^{-2}\,s^{-1}}$.

Table 3. Observational R Cas data and measured effective temperature.

Star	Date	$\Phi_{\rm vis}$	K [mag]	$F_{\rm bol}$ [10^{-8} erg/cm^2 s]	R^a [mas]	$T_{\rm eff}$ [K]
R Cas	99 August 29	0.08	-2.04	980.6±180	12.1±1.7	2685±238

Fig. 6 shows a comparison of measured and theoretical $T_{\rm eff,m}$-values. The theoretical and measured (phase 0.08) $T_{\rm eff}$-values are in agreement, within the 1σ error bar, with the E models at near-maximum phases 1.0 and 1.21, with the P models at phases 2.0 and 4.0, and with the M models at phases 1.0 and 2.0. Table 3 lists the measured bolometric flux, the average measured angular Rosseland radius R^a (see Sect. 4.2) and the average measured effective

temperature of R Cas. The average measured effective temperature and angular Rosseland radius is the average over all $T_{\rm eff,m}$- and $R^a_{\rm m}$-values corresponding to m-values with phases close to the phase of our observations (i.e., m = 1, 3, 6, 9, 11, 13, 15, 17, 19, 22 were used for averaging).

4.5. Pulsation mode

Adopting the above (Sect. 4.3) phase-averaged (over models M and P at near-maximum phases) linear Rosseland radius of the non-pulsating parent star, $R_{\rm p}$, of $240\,{\rm R}_\odot \pm 59\,{\rm R}_\odot$ for R Cas (derived from the measured R and the theoretical ratios given in Table 2), we find for the pulsation constant $Q = P\,(M/M_\odot)^{1/2}\,(R/R_\odot)^{-3/2}$ a value of Q=0.116±0.042 for a $1\,{\rm M}_\odot$ Mira with period P=430 days. This Q value agrees within the 1σ error with the theoretical value (Q=0.097) for fundamental pulsation mode for $1\,{\rm M}_\odot$ AGB stars with a period of $\sim$430 days (Fox & Wood [25]). The corresponding Q value of first overtone pulsation mode is Q=0.056. Note, however, that no direct measurement of a Mira mass exists and that a 20% uncertainty of M would for example result in a 10% uncertainty of Q.

5. CONCLUSION

We have observed the Mira star R Cas with the GI2T/REGAIN interferometer and our new infrared beam combiner. A uniform-disk (UD) K-band (2.1 μm) diameter of $25.3\,{\rm mas} \pm 3.3\,{\rm mas}$ was derived from the interferograms obtained with baselines between 12.0 m and 13.9 m at near-maximum variability phase 0.08. The unusually high visibility values at baselines 18.1 m, 19.8 m, 22.0 m, and 23.8 m show that the stellar surface of R Cas is more complex than previously assumed. Some of the theoretical models discussed above have an unusual wing-like visibility shape (e.g., P76200 in HSW98). Huge convection cells (predicted by Schwarzschild [26]) could also explain the observed visibility function. The visibility function of R Leo observed by Perrin et al. [15] with the IOTA interferometer has a similar wing-like shape as the R Cas visibility. Perrin et al. discuss several physical phenomena which may explain the excess of visibility at high frequencies.

The R Cas UD diameter measured at wavelength 1.04 μm at near-minimum phase 0.63 is $29.9\,{\rm mas} \pm 3.0\,{\rm mas}$ (HBSW2000 [16]), i.e., considerably larger than the above $25.3\,{\rm mas} \pm 3.3\,{\rm mas}$ UD diameter measured at 2.1 μm at near-maximum phase 0.08. The reason for this difference is not known and unexpected from the theoretical models discussed in the previous sections. The different variability phase of the two observations and/or other unknown effects, for example time-variable surface structure (e.g., supergranulation [26]), are possibly the cause of the diameter difference.

An angular R Cas Rosseland radius R^a of $12.1\,{\rm mas} \pm 1.7\,{\rm mas}$ at phase 0.08 was derived from the 2.1 μm visibilities measured with projected baselines between 12.0 m and 13.9 m by fitting theoretical center-to-limb variation profiles of five recent Mira star models (BSW96, HSW98). From the above mentioned 1.04 μm observation an angular Rosseland radius R^a of 16.5 mas±1.7 mas at phase 0.63 (HBSW2000), which is larger than the the near-maximum Rosseland radius reported in this paper, was obtained (HBSW2000; see above discussion).

The effective temperature of $2685\,{\rm K} \pm 238\,{\rm K}$ at near-maximum phase 0.08 was derived from the measured angular Rosseland radius and JHKLM-photometry carried out only seven days after the visibility observations.

For R Cas a good HIPPARCOS parallax ($9.36\,{\rm mas} \pm 1.10\,{\rm mas}$) is available and it is therefore possible to compare measured linear Rosseland and stellar filter radii with the theoretical radii of the BSW96 and HSW98 models. The measured radii were derived by fitting theoretical (BSW96, HSW98) center-to-limb intensity variations to the low-frequency visibility data. In the following table we compare measured and theoretical values:

Measured linear Rosseland R Cas radii R:	286±51 R$_\odot$	(M model*);	264±82 R$_\odot$	(P model**)
Theoretical linear Rosseland radii R:	315 R$_\odot$	(M model*);	263 R$_\odot$	(P model**)
Measured linear stellar K-band R Cas radii $R_{\rm K}$:	277±50 R$_\odot$	(M model*);	252±68 R$_\odot$	(P model**)
Theoretical linear stellar K-band radii $R_{\rm K}$:	304 R$_\odot$	(M model*);	259 R$_\odot$	(P model**)
Measured effective R Cas temperature:	2621±217 K	(M model*);	2797±275 K	(P model**)
Theoretical effective temperature:	2700 K	(M model*);	3030 K	(P model**)

(* average over phases 1.0, 2.0; ** average over phases 1.0, 2.0, 3.0, 4.0; derived from visibilities measured at baselines between 12.0 m and 13.9 m)

The comparison of these K-band (2.1 μm) observations with theoretical models suggests that R Cas is well represented by the fundamental mode M and P model (BSW96, HSW98), whereas the above mentioned 1.04 μm observations

suggested first-overtone pulsation. However, observations in more filters than just one continuum filter may be necessary for safely distinguishing a well-fitting model from an accidental match (cf. Ref. 16).

6. REFERENCES

1. M.S. Bessell, M. Scholz, P.R. Wood, *A&A* **307**, pp. 481, 1996 (BSW96)
2. K.-H. Hofmann, M. Scholz, P.R. Wood, *A&A* **339**, pp. 846, 1998 (HSW98)
3. A. Labeyrie, G. Schumacher, M. Dugue, C. Thom, P. Bourlon, F. Foy, D. Bonneau, R. Foy,
A&A **162**, pp. 359, 1986
4. D. Mourard, I. Tallon-Bosc, A. Blazit, D. Bonneau, G. Merlin, F. Morand, F. Vakili, A. Labeyrie,
A&A **283**, pp. 705, 1994
5. D. Bonneau, A. Labeyrie, *ApJ* **181**, pp. L1, 1973
6. A. Labeyrie, L. Koechlin, D. Bonneau, A. Blazit, R. Foy, *ApJ* **218**, pp.L75, 1977
7. D. Bonneau, R. Foy, A. Blazit, A. Labeyrie, *A&A* **106**, pp. 235, 1982
8. M. Karovska, P. Nisenson, C. Papaliolios, R.P. Boyle, *ApJ* **374**, pp. L51, 1991
9. C.A. Haniff, A.M. Ghez, P.W. Gorham, et al., *AJ* **103**, pp. 1662, 1992
10. A. Quirrenbach, D. Mozurkewich, J.T. Armstrong, et al., *A&A* **259**, pp. L19, 1992
11. R.W. Wilson, J.E. Baldwin, D.F. Buscher, P.J. Werner, *MNRAS* **257**, pp. 369, 1992
12. P.G. Tuthill, C.A Haniff, J.E. Baldwin, in: Very high angular resulution imaging,
IAU Symp.158, Robertson J.G., Tango W.J. (eds.), Kluwer, Dordrecht, p.395, 1994
13. C.A. Haniff, M. Scholz, P.G. Tuthill, *MNRAS* **276**, pp. 640, 1995
14. G. Weigelt, Y. Balega, K.-H. Hofmann, M. Scholz, *A&A* **316**, pp. L21, 1996
15. G. Perrin, V. Coudé du Foresto, S.T. Ridgway, et al., *A&A* **345**,
pp. 221, 1999
16. K.-H. Hofmann, Y. Balega, M. Scholz, G. Weigelt, *A&A* **353**, pp. 1016, 2000
17. T. Watanabe, K. Kodaira, *PASJ* **31**, pp. 61, 1979
18. M. Scholz, *A&A* **145**, pp. 251, 1985
19. M.S. Bessell, J.M. Brett, M. Scholz, P.R. Wood, *A&A* **213**, pp. 209, 1989
20. D. Mourard, I. Tallon-Bosc, F. Rigal, F. Vakili, D. Bonneau, F. Morand, Ph. Stee,
A&A **288**, pp. 675, 1994
21. D. Mourard, J.-M. Clausse, R. Dalla, M. Dugui, L. Koechlin, G. Merlin, E. Pedretti and M. Pierron,
"The GI2T/REGAIN control system and data reduction package", this proceedings
22. D. Mourard, D. Bonneau, A. Glentzlin, G. Merlin, R. Petrov, M. Pierron, N. Thureau and L. Abe, A. Blazit,
O. Chesneau, P. Stee, S. Ragland, F. Vakili, C. Virinaud, "The GI2T/REGAIN interferometer", this proceedings
23. M. Scholz, Y. Takeda, *A&A* **186**, pp. 200, 1987 (erratum: 196, 342)
24. F. Van Leeuwen, M.W. Feast, P.A. Whitelock, B. Yudin, *MNRAS* **287**, pp. 955, 1997
25. M.W. Fox, P.R. Wood, *ApJ* **259**, pp. 198, 1982
26. M. Schwarzschild, *ApJ* **195**, pp. 137, 1975